Effects of iron on the lattice thermal conductivity of Earth's deep mantle and implications for mantle dynamics

HPSTAR 540-2018

Wen-Pin Hsieh[a,1], Frédéric Deschamps[a], Takuo Okuchi[b], and Jung-Fu Lin[c,1]

[a]Institute of Earth Sciences, Academia Sinica, Nankang, 11529 Taipei, Taiwan; [b]Institute for Planetary Materials, Okayama University, Misasa, 682-0193 Tottori, Japan; and [c]Department of Geological Sciences, Jackson School of Geosciences, University of Texas at Austin, Austin, TX 78712-0254

Edited by Ho-kwang Mao, Carnegie Institution for Science, Washington, DC, and approved March 7, 2018 (received for review October 23, 2017)

Iron may critically influence the physical properties and thermochemical structures of Earth's lower mantle. Its effects on thermal conductivity, with possible consequences on heat transfer and mantle dynamics, however, remain largely unknown. We measured the lattice thermal conductivity of lower-mantle ferropericlase to 120 GPa using the ultrafast optical pump-probe technique in a diamond anvil cell. The thermal conductivity of ferropericlase with 56% iron significantly drops by a factor of 1.8 across the spin transition around 53 GPa, while that with 8–10% iron increases monotonically with pressure, causing an enhanced iron substitution effect in the low-spin state. Combined with bridgmanite data, modeling of our results provides a self-consistent radial profile of lower-mantle thermal conductivity, which is dominated by pressure, temperature, and iron effects, and shows a twofold increase from top to bottom of the lower mantle. Such increase in thermal conductivity may delay the cooling of the core, while its decrease with iron content may enhance the dynamics of large low shear-wave velocity provinces. Our findings further show that, if hot and strongly enriched in iron, the seismic ultralow velocity zones have exceptionally low conductivity, thus delaying their cooling.

ferropericlase | thermal conductivity | geodynamics | large low shear-wave velocity provinces | ultralow velocity zones

The large low shear-wave velocity provinces (LLSVPs) mapped at the bottom of the Earth's mantle are most likely hot, chemically differentiated regions (1), and their chemical component is best explained by an enrichment in iron (2, 3). It has further been suggested that the seismic ultralow velocity zones (ULVZs) observed on the core–mantle boundary (CMB) (4, 5) consist of thin pockets of strongly iron-rich materials (6, 7). The presence of iron in host minerals in the deep lower mantle can significantly influence the physical and chemical properties of these regions (8, 9), including their density, sound velocity, and transport and rheological properties. Iron further affects lower-mantle thermal conductivity, which in turn, may alter mantle dynamics and heat transfer. The influence of iron on the lower-mantle thermal conductivity operates at several different levels. Of particular interest are variations in global iron fraction (i.e., the total amount of iron oxide in mantle aggregate), the pressure-induced spin transition (10, 11), and changes in iron partitioning between bridgmanite (Bm) and ferropericlase (Fp), the two dominant minerals in the lower mantle (11, 12). Specifically, lateral variations in iron fraction at the lowermost mantle could change the lattice thermal conductivity of the region, as iron content in candidate lower-mantle minerals has been shown to influence their thermal conductivities. Moreover, the softening of bulk sound velocity (V_Φ) across the spin transition of iron (8, 13, 14) at the middle part of the lower mantle may influence the thermal conductivity as well, since the lattice thermal conductivity scales approximately with V^2, where V is the sound velocity including longitudinal and transverse velocities, based on a simplified classic model for the thermal transport (15). Precise determination of the effects of iron substitution and spin transition on the thermal conductivity of candidate lower-mantle materials would, therefore, provide critical insights into the thermal state and dynamics of the lower mantle (16), and into the heat transfer across the CMB (17).

The lattice and radiative thermal conductivities of constituent lower-mantle materials transfer heat by different mechanisms and thus, could play distinct roles in controlling the heat flux and thermal gradient in the deep lower mantle. Typically, the lattice thermal conductivity increases with pressure but decreases with temperature; however, the radiative thermal conductivity shows an opposite trend and is often assumed to be more important than the lattice component at high pressure–temperature (P-T) conditions in the lowermost mantle. The radiative thermal conductivity is largely influenced by the electronic structure of a material, but optical absorption spectroscopic measurements (18, 19) showed that the spin transition has little effect on the Fp radiative conductivity at lower-mantle conditions. On the contrary, as precise and reliable measurements remain a great challenge, little is known about the lattice thermal conductivity of lower-mantle materials under relevant P-T conditions, especially the effects of iron substitution and spin transition. Therefore, current understanding of the lower-mantle–lattice thermal conductivity has been largely based on theoretical calculations (20–24) or simplified model extrapolations using results at

Significance

Presence of iron in Earth's lower mantle may critically affect its physical properties and thermochemical structures. However, its effects on thermal conductivity and dynamics of deep mantle remain unknown. We studied lattice thermal conductivity of lower-mantle ferropericlase to 120 GPa using ultrafast optics. We observed an enhanced iron substitution effect in the low-spin iron-rich ferropericlase, with thermal conductivity that significantly drops across spin transition. Combined with bridgmanite data, we provided a self-consistent radial profile of lower-mantle thermal conductivity, which is dominated by pressure, temperature, and iron effects and shows a twofold increase throughout the lower mantle. If ultralow velocity zones are hot and strongly enriched in iron, their exceptionally low thermal conductivity will delay their cooling, influencing lowermost mantle dynamics.

Author contributions: W.-P.H. and J.-F.L. designed research; W.-P.H. and F.D. performed research; T.O. and J.-F.L. synthesized the samples; W.-P.H. and T.O. contributed new reagents/analytic tools; W.-P.H. analyzed data; and W.-P.H., F.D., and J.-F.L. wrote the paper.

The authors declare no conflict of interest.

This article is a PNAS Direct Submission.

[1]To whom correspondence may be addressed. Email: wphsieh@earth.sinica.edu.tw or afu@jsg.utexas.edu.

This article contains supporting information online at www.pnas.org/lookup/suppl/doi:10.1073/pnas.1718557115/-/DCSupplemental.

Published online April 2, 2018.

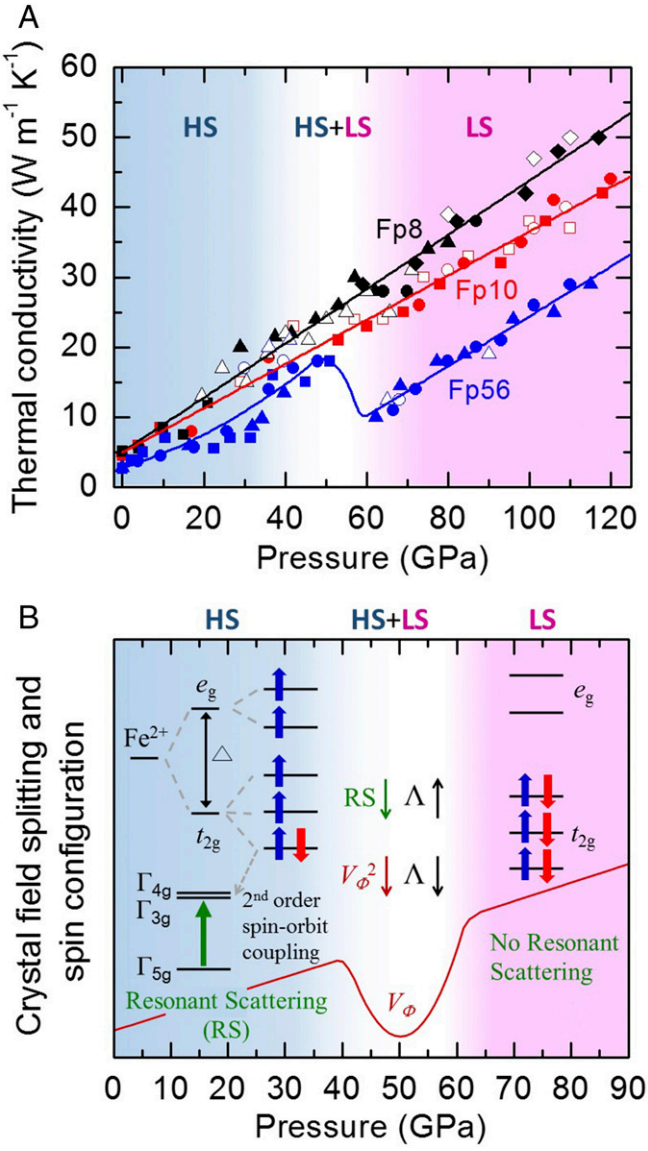

Fig. 1. Pressure evolution of the lattice thermal conductivity and physical mechanisms in Fp. (*A*) Lattice thermal conductivity of Fp at high pressures and room temperature. Within experimental uncertainties, the thermal conductivity of both Fp8 (black symbols) and Fp10 (red symbols) shows a monotonic increase with pressure. The thermal conductivity of Fp56 (blue symbols), however, presents very different pressure evolution and abruptly drops by a factor of ∼1.8 between 53 and 62 GPa. Each set of symbol shapes represents an individual measurement run, with colored symbols for compression cycle and white symbols for decompression cycle. The experimental uncertainties for the conductivity are ∼10% before 30 GPa, ∼20% at 60 GPa, and ∼25% at 120 GPa. The blue and red shaded areas represent the pressure ranges where Fe^{2+} ions are in the high-spin (HS) and low-spin (LS) states, respectively, while the faded region in between indicates the spin transition zone with mixed spin states (HS + LS). Solid curves are plotted to guide the eyes. (*B*) Schematic illustrations for the pressure evolution of thermal conductivity due to resonant scattering (RS) and softening of bulk sound velocity V_Φ across the spin transition. Crystal field splitting diagram and spin configuration of Fe^{2+} in HS and LS states are shown at the top. In HS state, the e_g energy levels are occupied by two spin-up electrons (blue arrows pointing up), and the t_{2g} levels are occupied by three spin-up electrons as well as one spin-down electron (red arrow pointing down). The second-order spin–orbit coupling further splits the t_{2g} energy levels into the Γ_{5g} and the nearly degenerate Γ_{4g} and Γ_{3g} states (30, 47). The transition between the Γ_{5g} and Γ_{4g}/Γ_{3g} states (labeled by the green arrow) gives rise to the RS that suppresses the phonon transport. During the spin transition (i.e., in the HS + LS zone), the thermal conductivity Λ is expected to be enhanced as the RS gradually decreases, while the V_Φ (red curve) softens; this results in a decrease in Λ, since Λ scales approximately with the square of sound velocity *V*, which includes longitudinal and transverse velocities. These two effects compete with each other and determine the evolution of thermal conductivity during the spin transition. In the LS state, the e_g levels become empty, and the t_{2g} levels are fully occupied by three paired electrons, leading to the disappearance of the RS.

relatively low *P-T* conditions without consideration of the effects of iron substitution and spin transition. Recently, experimental measurements of the lattice thermal conductivities of MgO periclase to 60 GPa (25) as well as Fp below 30 GPa (26, 27) and to 111 GPa (28) have been reported, but the results on Fp significantly differ at pressures above 20 GPa. Specifically, Ohta et al. (28) reported that the thermal conductivity of Fp with 19 mol % iron begins to decrease with pressure around 20–25 GPa and remains low at higher pressures. The anomalous pressure response was attributed to the spin transition of iron in Fp (28), while its onset pressure is much lower than the typical pressure range of the spin transition at ∼40–60 GPa (8). These results could not be simply explained using the aforementioned V^2 scaling based on experimental elasticity across the spin transition and in the low-spin state (8, 13). Thus far, the impacts of iron fraction anomaly and pressure-induced spin transition on the Fp lattice thermal conductivity at lowermost mantle *P-T* conditions remain poorly understood.

Here, we have combined ultrafast time domain thermoreflectance with a diamond anvil cell to measure the lattice thermal conductivity of single-crystal Fp with several iron contents—$Mg_{0.92}Fe_{0.08}O$ (Fp8), $Mg_{0.9}Fe_{0.1}O$ (Fp10), and $Mg_{0.44}Fe_{0.56}O$ (Fp56)—up to pressures near the lowermost mantle at room temperature. We further combined experimental results on the thermal conductivities of Bm (29) and Fp across the spin transition in various iron contents and iron partitioning in a pyrolytic mantle along representative lower-mantle *P-T* profiles to model thermal conductivity profiles and heat transfer in the deep mantle, offering insight into the lowermost mantle dynamics, in particular the evolution of iron-rich ULVZs.

Thermal Conductivity Across the Spin Transition

The lattice thermal conductivity of Fp8 (black symbols in Fig. 1*A*) at ambient pressure, 5.1 W m^{-1} K^{-1}, is smaller than that of MgO periclase by a factor of ∼10 due to the strong iron substitution effect, in which the phonon-defect scattering and the resonant spin-phonon scattering (30) substantially suppress the thermal phonon transport (*SI Text* has detailed discussions). Upon compression, the Fp8 thermal conductivity increases monotonically with increasing pressure to 50 W m^{-1} K^{-1} at 117 GPa. With increasing iron content, the enhanced resonant spin-phonon scattering and phonon-defect scattering further reduce the thermal conductivity. Our results on Fp10 show a slightly smaller ambient value, 4.5 W m^{-1} K^{-1}, and smaller monotonically increasing rate with pressure, reaching 44 W m^{-1} K^{-1} at 120 GPa (red symbols in Fig. 1*A*). These observations are in good agreement with previous results (27) (orange circles in Fig. S1) before 20 GPa, after which the literature data, however, increase drastically with large uncertainty. We did not observe significant, abrupt changes in the thermal conductivity of Fp8 and Fp10 across the pressure range of the spin transition, ∼40–60 GPa (8) (faded region labeled HS + LS in Fig. 1*A*), presumably due to the similar magnitudes of the competing effects of the bulk sound velocity softening and resonant spin-phonon scattering on the conductivity (Fig. 1*B* and *SI Text*).

Experimental results for Fp56, however, show distinct pressure dependence compared with Fp8 and Fp10 (blue symbols in Fig. 1*A*). The thermal conductivity of Fp56 at ambient condition is 2.8 W m^{-1} K^{-1} due to a significant amount of iron substitution,

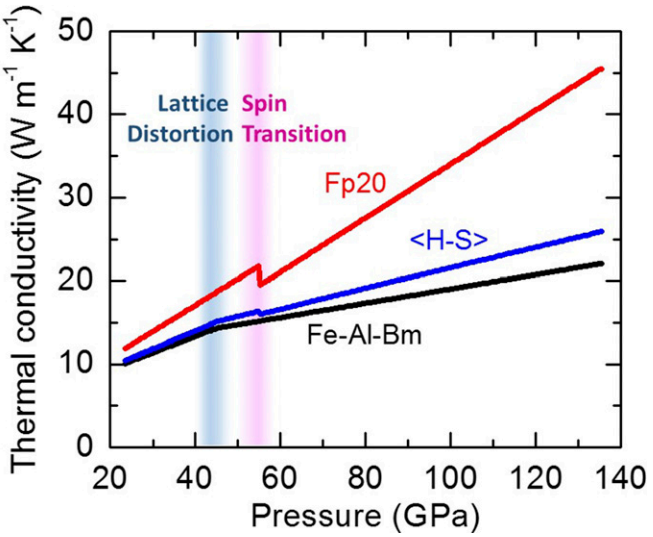

Fig. 2. Modeled lattice thermal conductivity of lower-mantle Fp and Bm at high pressures and room temperature. Thermal conductivity for Fp with an iron content of 20% (Fp20; red curve) is obtained by linear interpolation of our data shown in Fig. 1*A*. The data for Fe-Al-Bm (black curve) are a polynomial fit to the results by Hsieh et al. (29). We calculate the Hashin–Shtrikman average <H-S> (blue curve), defined as the geometric average of the lower and upper Hashin–Shtrikman bounds (*SI Text*), of the thermal conductivity for a lower-mantle aggregate made of 80% volume of Fe-Al-Bm and 20% volume of Fp20 in a simplified pyrolite mineralogical model. The blue and red shaded areas represent the pressure ranges where the pressure-induced lattice distortion occurs in Fe-Al-Bm and the spin transition occurs in Fp20, respectively.

and it increases with pressure until $P \sim 50$ GPa. Further compression results in a significant drop of the thermal conductivity by a factor of ~1.8 between 53 and 62 GPa, which can be associated with the spin transition. The spin transition zone is theoretically and experimentally known to result in softening of the bulk sound velocity (8), and it is shown here to play a key role in reducing the thermal conductivity (Fig. 1*B*). After the transition, the thermal conductivity of the low-spin Fp increases monotonically to 29 W m^{-1} K^{-1} at 115 GPa, ~40% smaller than Fp8 at similar pressure. In contrast to the iron substitution effect in the high-spin Fp, the iron substitution effect is drastically enhanced in the low-spin state due to the stronger phonon-defect scattering and larger magnitude of the softening of bulk sound velocity across the spin transition. The enhanced iron substitution effect in the low-spin Fp that we observe here may result in an exceptionally low thermal conductivity in iron-rich regions at the lowermost mantle that was proposed to be a source of the ULVZs (31) (modeling and discussions are given below).

Modeling Lower-Mantle Thermal Conductivity

In Fig. 2, we summarize our high-pressure, room temperature lattice thermal conductivities of major candidate lower-mantle minerals with relevant Fe and Al contents in the lower mantle [i.e., (Fe,Al)-bearing bridgmanite (Fe-Al-Bm) (black curve in Fig. 2) taken from ref. 29 and Fp20 (red curve in Fig. 2)]. The thermal conductivity of Fp20 is linearly interpolated from our data shown in Fig. 1*A* for an iron content of 20% and shows a small discontinuity of ~10%, smaller than our measurement uncertainty, around 50–60 GPa due to the spin transition in Fp (*SI Text* has details). Our results on the Fp20 and Fe-Al-Bm enable us to further calculate the lattice thermal conductivity of the lower-mantle mineral aggregate at high pressure and room temperature. For simplicity, we assume that the lower mantle is composed of a simplified pyrolite compositional model containing Fe-Al-Bm with a proportion of 80% in volume and Fp20 with 20% in volume (8). We then calculate Hashin–Shtrikman bounds of aggregate thermal conductivity, which are the narrowest bounds for a multiphase system, and take the geometric average of these bounds as an estimator of lower-mantle thermal conductivity (blue curve in Fig. 2; *SI Text* has details). The pressure derivative is slightly reduced around 45 GPa due to the smaller increasing rate of Fe-Al-Bm thermal conductivity with pressure, which results itself from the pressure-induced lattice distortion on the iron sites (29). Again, a small discontinuity around 50–60 GPa is caused by the spin transition in Fp20. Note that the aggregate thermal conductivity is dominated by the Bm thermal conductivity due to its dominant volume fraction in the lower mantle. Changes in the Fp thermal conductivity triggered by the spin transition and the potential variation of the onset pressure and range of the spin transition with different iron content play a relatively minor role in affecting the lower-mantle aggregate thermal conductivity.

To model the lattice thermal conductivity at relevant lower-mantle compositional and *P-T* conditions, we further consider integrated effects of pressure, temperature, and iron partitioning (K_D) between Bm and Fp as well as the pressure-induced spin transition in Fp and pressure-induced lattice distortion in Bm due to the Fe and Al substitutions (*SI Text* has details). Note that our modeling here does not account for potential iron saturation effects, where the thermal conductivity saturates when the iron content is larger than a threshold value, for which no experimental data are available to indicate its existence to date. For applications to the typical lower mantle and LLSVPs, where global iron content should be in the range of 8–12%, the iron saturation effects may be very limited (*SI Text*), if occurring at all, and therefore, should not alter our conclusions. By contrast, in regions strongly enriched in iron, as is possibly the case for ULVZs, saturation effects should be accounted for (see below). In Fig. 3, we plot lower-mantle thermal conductivity at three

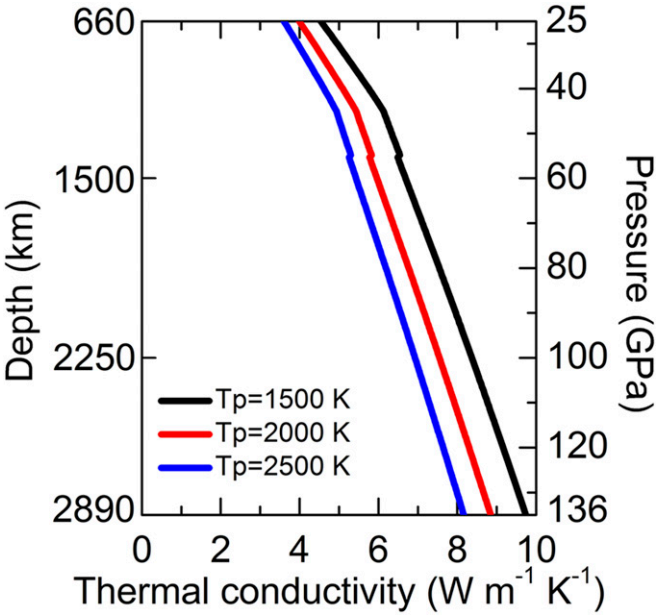

Fig. 3. Lattice thermal conductivity of a representative lower-mantle mineral aggregate at high pressures and temperatures. We use Hashin–Shtrikman average for the thermal conductivity by considering integrated effects of pressure, temperature, iron partitioning, iron spin transition, and lattice distortion. Bm volume fraction of 0.8, global iron fraction of 0.09, a depth-dependent iron partitioning coefficient by Irifune et al. (12), and the temperature effect of $T^{-1/2}$ dependence are used to model the mantle thermal conductivity. Data for Bm are from Fe-Al-Bm (29). The small discontinuity around 50–60 GPa is caused by the spin transition of iron in Fp.

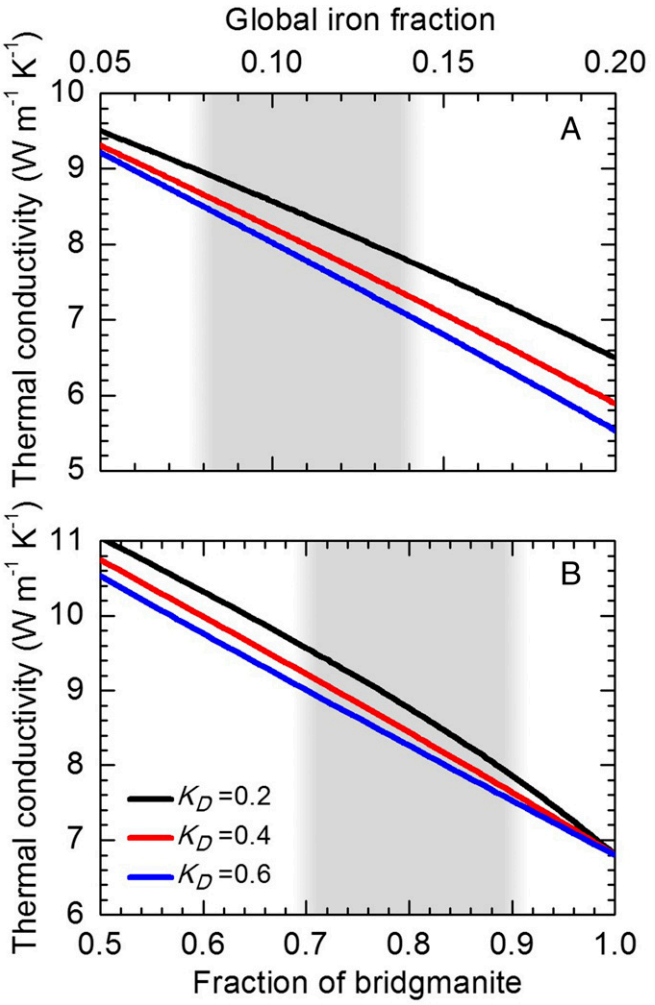

Fig. 4. Thermal conductivity of a representative lower-mantle mineral aggregate as a function of (*A*) global iron fraction and (*B*) fraction of Bm, with different iron partitioning coefficient at the lowermost mantle conditions. Calculations are made for a representative temperature T = 3,000 K at a depth of 2,800 km (P = 130.2 GPa). In *A*, the fraction of Bm is set to X_{Bm} = 0.8, and in *B*, the global iron fraction is set to X_{Fe} = 0.09. Data for Bm are from Fe-Al-Bm (29). The effect of the spin transition in Fp, which results in a small discontinuity in the thermal conductivity around 50–60 GPa, is included. Gray shaded areas represent expected variations in the fractions of global iron and Bm in the lowermost mantle.

different potential temperatures assuming that the temperature dependences of the Bm and Fp both follow the typical $T^{-1/2}$ dependence (25, 32, 33). Changes in K_D with depth were taken from the work by Irifune et al. (12). Our modeling shows that thermal conductivity increases by about a factor of two from top to bottom of the lower mantle. A variation of temperature by 500 K, typical of the lateral anomalies expected in the lowermost mantle (3), induces a change in thermal conductivity of ∼1 W m^{-1} K^{-1} (i.e., ∼12% of the estimated aggregate conductivity). Fig. 4 further quantifies the influences of the global iron content (X_{Fe}) and fraction of Bm (X_{Bm}) on lower-mantle thermal conductivity. Varying either X_{Fe} by 4% or X_{Bm} by 10%, as is expected in the lowermost mantle (3), again leads to a change in thermal conductivity of ∼1 W m^{-1} K^{-1}. By contrast, as shown in Figs. S5 and S6, spin transition in Fp and variations of K_D with depth play relatively minor roles in affecting lower-mantle thermal conductivity. Although our calculations are based on extrapolations of room temperature data, variations of the lower-mantle thermal conductivity profiles shown in Fig. 3 due to changes in the onset pressure and range of spin transition at high temperatures are small. Finally, we note that the lattice thermal conductivity in the lowermost mantle is constrained to ∼8 W m^{-1} K^{-1} (Fig. 3), larger than the available experimental data for the lower-mantle radiative thermal conductivity (34, 35), ∼0.5–3 W m^{-1} K^{-1}, at similar *P-T* conditions, indicating the lattice conductivity mainly contributes to the heat transfer in Earth's deep lower mantle.

Consequences on Deep-Mantle Dynamics and Evolution

The combination of our data for Fp and previous measurements for Fe-Al-Bm (29) allows us to build self-consistent radial profiles of lower-mantle thermal conductivity that account for pressure, thermal, and compositional effects. While it may not drastically alter mantle convection, a twofold increase of thermal conductivity with depth throughout the lower mantle may, according to purely thermal simulations of mantle convection

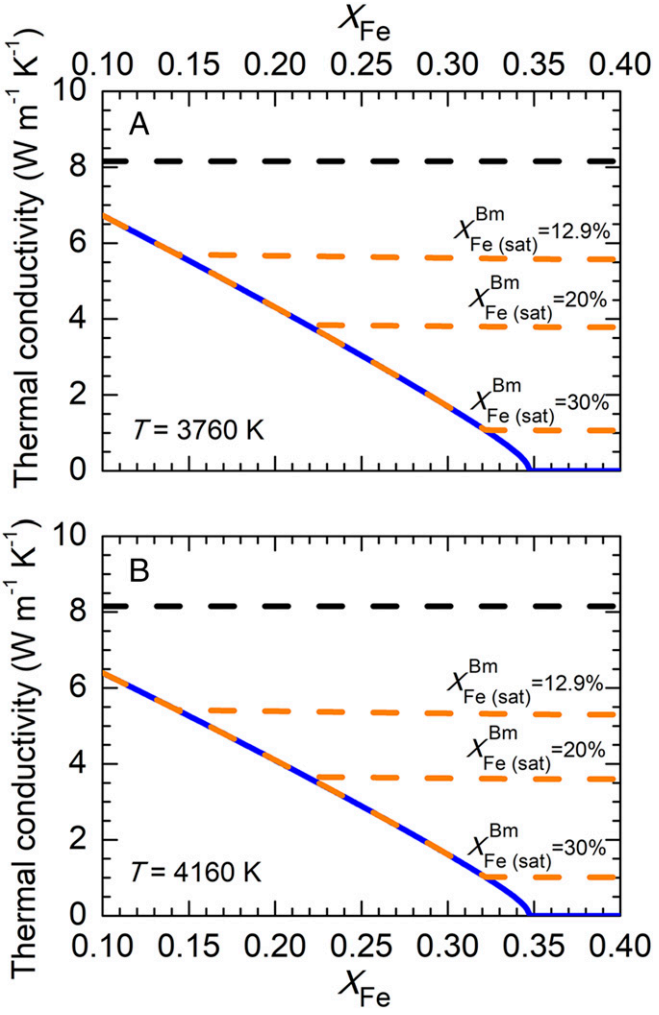

Fig. 5. Thermal conductivity for hot, iron-rich aggregate at the bottom of the mantle, representing seismic ULVZs. Calculations are made at a depth of z = 2,880 km (P = 134.7 GPa), iron partitioning K_D = 0.4, fraction of Bm X_{Bm} = 0.9, and real temperatures of (*A*) T = 3,760 K and (*B*) T = 4,160 K. Results are plotted as a function of the global fraction of iron, X_{Fe}. In each plot, the thick horizontal dashed line shows the thermal conductivity at the bottom of the mantle along a geotherm T_p = 2,500 K (T = 3,360 K) and for an aggregate with X_{Bm} = 0.8 and X_{Fe} = 0.09, representative of the average lower mantle (blue curve in Fig. 3). Blue curves do not account for possible iron saturation effects and would unphysically go to zero for X_{Fe} ∼ 0.35. Orange dashed curves account for iron saturation in Bm with different threshold values (labels on curves) and iron saturation in Fp with a threshold value $x^{Fp}_{Fe(sat)}$ = 56%.

(36), delay the cooling of the core. In thermochemical simulations, a twofold increase helps stabilize reservoirs of chemically differentiated materials at the bottom of the system (37) and may affect the distribution of plumes in the deep mantle (38). In particular, the number of plumes generated outside the thermochemical reservoirs is reduced, and their spacing is increased, in agreement with seismic observations (38). By contrast, the consequences of thermal conductivity changes due to compositional variations on mantle convection have, so far, not been investigated. If, as suggested by probabilistic tomography (3), LLSVPs are hotter than average by about 400–500 K and enriched in iron by ∼3%, their thermal conductivity might be lower than that of surrounding mantle by ∼20%, affecting, in turn, their dynamics. Finally, it has been suggested that, because it triggers a change in density, the spin transition in Fp, which is responsible for the reduction of thermal conductivity that we observed in Fp56, may affect mantle dynamics (39–42). Potential effects include enhanced flow velocities (39–41), allowing cold downwelling to spread more easily around the CMB, and the destabilization of reservoirs of dense material (42). The exact amplitude of these effects is, however, still debated. Although the decrease in lower-mantle thermal conductivity induced by the spin transition has not yet been included in numerical simulations of convection, the amplitude of this decrease is small (Fig. S5), and its impact on lower-mantle dynamics may thus be limited (41).

Because thermal conductivity is partially controlling the heat flux at the CMB, lateral variations in thermal conductivity related to variations in temperature and iron fraction may further influence core dynamics and geodynamo. Previous calculations using recent data for thermal conductivity of Bm (29) indicate that, while heat flux is mostly controlled by thermal pattern at the CMB, the lateral variations in thermal conductivity still play a significant role. Our data for Fp would increase this effect.

Our findings may further have strong implications for the evolution of the ULVZs observed at the bottom of the mantle (4, 5). Several explanations have been proposed for their structures, including pockets of partial melting (43) and patches of materials enriched in iron oxides, in particular iron-rich Fp (31), subducted banded iron formation (44), and postperovskite (45). The detailed geographical distribution of ULVZs may provide hints about their nature: recent geodynamic modeling (7) suggests that ULVZs would be preferentially located well within LLSVPs if they are related to partial melt, while they would be concentrated along the edges of LLSVPs if they consist of chemically denser (e.g., iron-rich) materials. While a full seismic coverage of the CMB region has not yet been completed, available seismic observations indicate that ULVZs are preferentially located within or at the edges of LLSVPs (46) (i.e., in regions likely hotter than average mantle). Compared with average lower mantle, ULVZs may thus be simultaneously hotter and strongly enriched in iron. Following this hypothesis, their thermal conductivity would be strongly reduced. This low conductivity would be further reduced by a possible enrichment in Bm, as LLSVPs may be enriched in Bm (3). For instance, taking $K_D = 0.4$, $X_{Bm} = 0.9$, and a temperature of 3,760 K (i.e., ∼400 K higher than the bottom temperature for a potential geotherm $T_p = 2{,}500$ K), modeling of our measurements predicts a thermal conductivity of ∼6.3 W m^{-1} K^{-1} for an enrichment in iron of 3% compared with pyrolitic composition (i.e., $X_{Fe} = 12\%$; corresponding to iron fractions in Bm and Fp of $x_{Fe}^{Bm} = 10.8\%$ and $x_{Fe}^{Fp} = 23.2\%$, respectively) and ∼1.7 W m^{-1} K^{-1} for an enrichment in iron of 21% ($X_{Fe} = 30\%$; corresponding to $x_{Fe}^{Bm} = 27.9\%$ and $x_{Fe}^{Fp} = 49.1\%$) (Fig. 5*A* and *SI Text*). These values are lower than the estimated thermal conductivity for the average lower mantle (blue curve in Fig. 3) by ∼23 and 80%, respectively. Therefore, if ULVZs started hotter and were strongly enriched in iron at the early stage of the Earth's interior, they may have had (and still have) a very low thermal conductivity compared with the surrounding mantle. This, in turn, may have delayed their cooling, allowing the persistence of small pockets of hot materials up to now. ULVZs may thus be substantially hotter than LLSVPs, further decreasing their thermal conductivity. Assuming that ULVZs are hotter than LLSVPs by 400 K (i.e., 800 K higher than a potential geotherm $T_p = 2{,}500$ K) and for $K_D = 0.4$ and $X_{Bm} = 0.9$, thermal conductivity for $X_{Fe} = 30\%$ is around 1.6 W m^{-1} K^{-1} (Fig. 5*B*). By contrast, a low thermal conductivity would enhance convection within ULVZs and thus, may accelerate their cooling, provided that these structures can be animated by convection. However, because ULVZs observed so far are thin elongated structures, it is not clear whether convection is able to operate within them. The hypothesis that ULVZs are strongly enriched in iron oxide implies that the fractions of iron in Bm and Fp reach high values: 20% or higher. Because our data for Bm (29) are limited to $x_{Fe}^{Bm} = 12.9\%$, extrapolation to higher values of x_{Fe}^{Bm} may be biased. This appears clearly in blue curves in Fig. 5, showing that thermal conductivity of the aggregate would unphysically go to zero for values of X_{Fe} ∼ 35%, corresponding to $x_{Fe}^{Bm} \sim 33\%$ for $K_D = 0.4$ and $X_{Bm} = 0.9$. Instead, the iron saturation effects may occur for values of x_{Fe}^{Bm} larger than a threshold value, $x_{Fe(sat)}^{Bm}$, limiting the decrease in thermal conductivity with increasing x_{Fe}^{Bm}. To date, however, there are no indications or experimental data constraining $x_{Fe(sat)}^{Bm}$ if the saturation effect is existing. To account for the possible iron saturation effects, we assumed several values of $x_{Fe(sat)}^{Bm}$ in the range of 12.9–30% (dashed orange curves in Fig. 5). Interestingly, in all cases, the thermal conductivity remains lower than the average lower-mantle conductivity by at least 30% for $x_{Fe(sat)}^{Bm} = 12.9\%$ and up to ∼80% for $x_{Fe(sat)}^{Bm} = 30\%$. Finally, it is important to note that our modeling implicitly assumes that the ULVZs are regions with solid materials strongly enriched in iron. For a given material, thermal conductivity is typically lower if this material is melted or partially melted than if it is a solid. Therefore, although the thermal conductivity of partially melted iron-rich materials at the lowermost mantle conditions remains largely unknown, it is expected to be lower than that of solid iron-rich materials. If ULVZs are composed of iron-rich partial melt, their cooling would thus be further delayed.

A significant decrease in thermal conductivity due to the combination of thermal and chemical (iron enrichment) effects is thus likely to affect the evolution of ULVZs if these regions are enriched in iron and to a lesser extent, the heat flux at CMB and the evolution of the core as well as the dynamics of LLSVPs. The detailed evolution and dynamics of ULVZs and LLSVPs remain to be investigated. Incorporating our experimental data for thermal conductivity of lower-mantle minerals in simulations of mantle dynamics may, therefore, bring insight into the combined evolution of the Earth's mantle and core.

ACKNOWLEDGMENTS. We thank J. Yang, N. Tomioka, and S. Jacobsen for help with synthesis and preparation of the samples; S. Jacobsen for sharing experimental parameters for synthesis of ferropericlase and bridgmanite; and V. Prakapenka for his assistance with X-ray diffraction analysis of the starting crystals. The work by W.-P.H. and F.D. was supported by the Academia Sinica and Ministry of Science and Technology of Taiwan, Republic of China Contracts CDA-106-M02 (to W.-P.H.), MOST 103-2112-M-001-001-MY3 (to W.-P.H.), 105-2116-M-001-024 (to W.-P.H.), 106-2116-M-001-022 (to W.-P.H.), 105-2116-M-001-017 (to F.D.), and AS-102-CDA-M02 (to F.D.). J.-F.L. acknowledges support from the Geophysics and Cooperative Studies of the Earth's Deep Interior Programs of the US National Science Foundation, the Visiting Professorship Program of the Institute for Planetary Materials, Okayama University, and the Center for High Pressure Science and Technology Advanced Research. This work was supported, in part, by Japan Society for the Promotion of Science KAKENHI Grant 26287135. X-ray diffraction patterns of the crystal were analyzed at GeoSoilEnviroCARS (GSECARS) sector of the Advanced Photon Source. GSECARS was supported by National Science Foundation Grant EAR-0622171 and Department of Energy Grant DE-FG02-94ER14466 under Contract DE-AC02-06CH11357. The APS is supported by 263 Department of Energy–Basic Energy Sciences Contract DE-AC02-06CH11357.

1. Garnero EJ, McNamara AK, Shim S-H (2016) Continent-sized anomalous zones with low seismic velocity at the base of Earth's mantle. *Nat Geosci* 9:481–489.
2. Deschamps F, Cobden L, Tackley PJ (2012) The primitive nature of large low shear-wave velocity provinces. *Earth Planet Sci Lett* 349–350:198–208.
3. Trampert J, Deschamps F, Resovsky J, Yuen D (2004) Probabilistic tomography maps chemical heterogeneities throughout the lower mantle. *Science* 306:853–856.
4. Wen L, Helmberger DV (1998) Ultra-low velocity zones near the core-mantle boundary from broadband PKP precursors. *Science* 279:1701–1703.
5. Thorne MS, Garnero EJ (2004) Inferences on ultralow-velocity zone structure from a global analysis of SPdKS waves. *J Geophys Res B Solid Earth* 109:1–22.
6. Mao WL, et al. (2004) Ferromagnesian postperovskite silicates in the D'' layer of the Earth. *Proc Natl Acad Sci USA* 101:15867–15869.
7. Li M, McNamara AK, Garnero EJ, Yu S (2017) Compositionally-distinct ultra-low velocity zones on Earth's core-mantle boundary. *Nat Commun* 8:177.
8. Lin J-F, Speziale S, Mao Z, Marquardt H (2013) Effects of the electronic spin transitions of iron in lower mantle minerals: Implications for deep mantle geophysics and geochemistry. *Rev Geophys* 51:244–275.
9. Badro J (2014) Spin transitions in mantle minerals. *Annu Rev Earth Planet Sci* 42: 231–248.
10. Badro J, et al. (2004) Electronic transitions in perovskite: Possible nonconvecting layers in the lower mantle. *Science* 305:383–386.
11. Badro J, et al. (2003) Iron partitioning in Earth's mantle: Toward a deep lower mantle discontinuity. *Science* 300:789–791.
12. Irifune T, et al. (2010) Iron partitioning and density changes of pyrolite in Earth's lower mantle. *Science* 327:193–195.
13. Yang J, Tong X, Lin J-F, Okuchi T, Tomioka N (2015) Elasticity of ferropericlase across the spin crossover in the Earth's lower mantle. *Sci Rep* 5:17188.
14. Wu Z, Justo JF, Wentzcovitch RM (2013) Elastic anomalies in a spin-crossover system: Ferropericlase at lower mantle conditions. *Phys Rev Lett* 110:228501.
15. Ashcroft NW, Mermin ND (1976) *Solid State Physics* (Thomson Learning, Stamford, CT), p 500.
16. Lin J-F, et al. (2007) Spin transition zone in Earth's lower mantle. *Science* 317: 1740–1743.
17. Lay T, Hernlund J, Buffett BA (2008) Core–mantle boundary heat flow. *Nat Geosci* 1: 25–32.
18. Goncharov AF, Struzhkin VV, Jacobsen SD (2006) Reduced radiative conductivity of low-spin (Mg,Fe)O in the lower mantle. *Science* 312:1205–1208.
19. Keppler H, Kantor I, Dubrovinsky LS (2007) Optical absorption spectra of ferropericlase to 84 GPa. *Am Mineral* 92:433–436.
20. Tang X, Ntam MC, Dong J, Rainey ES, Kavner A (2014) The thermal conductivity of Earth's lower mantle. *Geophys Res Lett* 41:2746–2752.
21. Hofmeister AM (1999) Mantle values of thermal conductivity and the geotherm from phonon lifetimes. *Science* 283:1699–1706.
22. Haigis V, Salanne M, Jahn S (2012) Thermal conductivity of MgO, MgSiO3 perovskite and post-perovskite in the Earth's deep mantle. *Earth Planet Sci Lett* 355–356: 102–108.
23. Stackhouse S, Stixrude L, Karki BB (2010) Thermal conductivity of periclase (MgO) from first principles. *Phys Rev Lett* 104:208501.
24. Ammann MW, et al. (2014) Variation of thermal conductivity and heat flux at the Earth's core mantle boundary. *Earth Planet Sci Lett* 390:175–185.
25. Dalton DA, Hsieh W-P, Hohensee GT, Cahill DG, Goncharov AF (2013) Effect of mass disorder on the lattice thermal conductivity of MgO periclase under pressure. *Sci Rep* 3:2400.
26. Manthilake GM, de Koker N, Frost DJ, McCammon CA (2011) Lattice thermal conductivity of lower mantle minerals and heat flux from Earth's core. *Proc Natl Acad Sci USA* 108:17901–17904.
27. Goncharov AF, et al. (2015) Experimental study of thermal conductivity at high pressures: Implications for the deep Earth's interior. *Phys Earth Planet Inter* 247: 11–16.
28. Ohta K, Yagi T, Hirose K, Ohishi Y (2017) Thermal conductivity of ferropericlase in the Earth's lower mantle. *Earth Planet Sci Lett* 465:29–37.
29. Hsieh W-P, Deschamps F, Okuchi T, Lin J-F (2017) Reduced lattice thermal conductivity of Fe-bearing bridgmanite in Earth's deep mantle. *J Geophys Res Solid Earth* 122: 4900–4917.
30. Morton IP, Lewis MF (1971) Effect of iron impurities on the thermal conductivity of magnesium oxide single crystals below room temperature. *Phys Rev B* 3:552–559.
31. Wicks JK, Jackson JM, Sturhahn W (2010) Very low sound velocities in iron-rich (Mg,Fe)O: Implications for the core-mantle boundary region. *Geophys Res Lett* 37:L15304.
32. Klemens PG, White GK, Tainsh RJ (1962) Scattering of lattice waves by point defects. *Philos Mag* 7:1323–1335.
33. Xu Y, et al. (2004) Thermal diffusivity and conductivity of olivine, wadsleyite and ringwoodite to 20 GPa and 1373 K. *Phys Earth Planet Inter* 143:321–336.
34. Goncharov AF, Haugen BD, Struzhkin VV, Beck P, Jacobsen SD (2008) Radiative conductivity in the Earth's lower mantle. *Nature* 456:231–234.
35. Keppler H, Dubrovinsky LS, Narygina O, Kantor I (2008) Optical absorption and radiative thermal conductivity of silicate perovskite to 125 gigapascals. *Science* 322: 1529–1532.
36. van den Berg AP, Rainey ESG, Yuen DA (2005) The combined influences of variable thermal conductivity, temperature- and pressure-dependent viscosity and core-mantle coupling on thermal evolution. *Phys Earth Planet Inter* 149:259–278.
37. Tackley PJ (1998) *Three-Dimensional Simulations of Mantle Convection with a Thermo-Chemical CMB Boundary Layer: D"?*, Core-Mantle Boundary Region Geodynamics Series, ed Gurnis M (American Geophysical Union, Washington, DC), Vol 28, pp 231–253.
38. Li M, Zhong S (2017) The source location of mantle plumes from 3D spherical models of mantle convection. *Earth Planet Sci Lett* 478:47–57.
39. Bower DJ, Gurnis M, Jackson JM, Sturhahn W (2009) Enhanced convection and fast plumes in the lower mantle induced by the spin transition in ferropericlase. *Geophys Res Lett* 36:L10306.
40. Shahnas MH, Peltier WR, Wu Z, Wentzcovitch R (2011) The high–Pressure electronic spin transition in iron : Potential impacts upon mantle mixing. *J Geophys Res Solid Earth* 116:B08205.
41. Vilella K, Shim S, Farnetani CG, Badro J (2015) Spin state transition and partitioning of iron : Effects on mantle dynamics. *Earth Planet Sci Lett* 417:57–66.
42. Huang C, Leng W, Wu Z (2015) Iron-spin transition controls structure and stability of LLSVPs in the lower mantle. *Earth Planet Sci Lett* 423:173–181.
43. Williams Q, Garnero EJ (1996) Seismic evidence for partial melt at the base of Earth's mantle. *Science* 273:1528.
44. Dobson DP, Brodholt JP (2005) Subducted banded iron formations as a source of ultralow-velocity zones at the core-mantle boundary. *Nature* 434:371–374.
45. Mao WL, et al. (2006) Iron-rich post-perovskite and the origin of ultralow-velocity zones. *Science* 312:564–565.
46. McNamara AK, Garnero EJ, Rost S (2010) Tracking deep mantle reservoirs with ultra-low velocity zones. *Earth Planet Sci Lett* 299:1–9.
47. Wong JY (1968) Far-infrared spectra of iron-doped MgO. *Phys Rev* 168:337.
48. Mao HK, Bell PM, Shaner JW, Steinberg DJ (1978) Specific volume measurements of Cu, Mo, Pd, and Ag and calibration of the ruby R1 fluorescence pressure gauge from 0.06 to 1 Mbar. *J Appl Phys* 49:3276–3283.
49. Kang K, Koh YK, Chiritescu C, Zheng X, Cahill DG (2008) Two-tint pump-probe measurements using a femtosecond laser oscillator and sharp-edged optical filters. *Rev Sci Instrum* 79:114901.
50. Cahill DG (2004) Analysis of heat flow in layered structures for time-domain thermoreflectance. *Rev Sci Instrum* 75:5119–5122.
51. Ge Z, Cahill DG, Braun PV (2006) Thermal conductance of hydrophilic and hydrophobic interfaces. *Phys Rev Lett* 96:186101.
52. Schmidt A, Chiesa M, Chen X, Chen G (2008) An optical pump-probe technique for measuring the thermal conductivity of liquids. *Rev Sci Instrum* 79:064902.
53. Zheng X, Cahill DG, Krasnochtchekov P, Averback RS, Zhao JC (2007) High-throughput thermal conductivity measurements of nickel solid solutions and the applicability of the Wiedemann-Franz law. *Acta Mater* 55:5177–5185.
54. Chen B, Hsieh W-P, Cahill DG, Trinkle DR, Li J (2011) Thermal conductivity of compressed H_{2}O to 22 GPa: A test of the Leibfried-Schlömann equation. *Phys Rev B* 83: 132301.
55. Hsieh W-P, Chen B, Li J, Keblinski P, Cahill DG (2009) Pressure tuning of the thermal conductivity of the layered muscovite crystal. *Phys Rev B* 80:180302.
56. Hsieh W-P (2015) Thermal conductivity of methanol-ethanol mixture and silicone oil at high pressures. *J Appl Phys* 117:235901.
57. Fukui H, Tsuchiya T, Baron AQR (2012) Lattice dynamics calculations for ferropericlase with internally consistent LDA+U method. *J Geophys Res Solid Earth* 117:B12202.
58. Wu Z, Justo JF, DaSilva CRS, DeGironcoli S, Wentzcovitch RM (2009) Anomalous thermodynamic properties in ferropericlase throughout its spin crossover transition. *Phys Rev B* 80:14409.
59. Cahill DG, Watanabe F (2004) Thermal conductivity of isotopically pure and Ge-doped Si epitaxial layers from 300 to 550 K. *Phys Rev B* 70:235322.
60. Dziewonski AM, Anderson DL (1981) Preliminary reference Earth model. *Phys Earth Planet Inter* 25:297–356.
61. Hashin Z, Shtrikman S (1962) A variational approach to the theory of the effective magnetic permeability of multiphase materials. *J Appl Phys* 33:3125–3131.